

Water Cluster Confinement and Methane Adsorption in the Hydrophobic Cavities of a Fluorinated Metal–Organic Framework

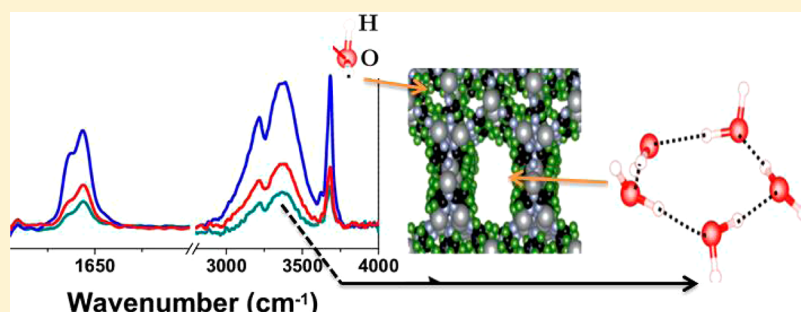
Nour Nijem,[†] Pieremanuele Canepa,[‡] Ushasree Kaipa,[§] Kui Tan,[†] Katy Roodenko,[†] Sammer Tekarli,[§] Jason Halbert,[§] Iain W. H. Oswald,[§] Ravi K. Arvapally,[§] Chi Yang,[§] Timo Thonhauser,[‡] Mohammad A. Omary,*[§] and Yves J. Chabal*,[†]

[†]Department of Materials Science and Engineering, University of Texas at Dallas, Texas 75080, United States

[‡]Department of Physics, Wake Forest University, Winston-Salem, North Carolina 27109, United States

[§]Department of Chemistry, University of North Texas, Denton, Texas 76203, United States

S Supporting Information



ABSTRACT: Water cluster formation and methane adsorption within a hydrophobic porous metal organic framework is studied by *in situ* vibrational spectroscopy, adsorption isotherms, and first-principle DFT calculations (using vdW-DF). Specifically, the formation and stability of H_2O clusters in the hydrophobic cavities of a fluorinated metal–organic framework (FMOF-1) is examined. Although the isotherms of water show no measurable uptake (see Yang et al. *J. Am. Chem. Soc.* 2011, 133, 18094), the large dipole of the water internal modes makes it possible to detect low water concentrations using IR spectroscopy in pores in the vicinity of the surface of the solid framework. The results indicate that, even in the low pressure regime (100 mTorr to 3 Torr), water molecules preferentially occupy the large cavities, in which hydrogen bonding and wall hydrophobicity foster water cluster formation. We identify the formation of pentameric water clusters at pressures lower than 3 Torr and larger clusters beyond that pressure. The binding energy of the water species to the walls is negligible, as suggested by DFT computational findings and corroborated by IR absorption data. Consequently, intermolecular hydrogen bonding dominates, enhancing water cluster stability as the size of the cluster increases. The formation of water clusters with negligible perturbation from the host may allow a quantitative comparison with experimental environmental studies on larger clusters that are in low concentrations in the atmosphere. The stability of the water clusters was studied as a function of pressure reduction and in the presence of methane gas. Methane adsorption isotherms for activated FMOF-1 attained volumetric adsorption capacities ranging from 67 V(STP)/V at 288 K and 31 bar to 133 V(STP)/V at 173 K and 5 bar, with an isosteric heat of adsorption of ca. 14 kJ/mol in the high temperature range (288–318 K). Overall, the experimental and computational data suggest high preferential uptake for methane gas relative to water vapor within FMOF-1 pores with ease of desorption and high framework stability under operative temperature and moisture conditions.

1. INTRODUCTION

Water nanoconfinement in proteins, carbon nanotubes, and fullerenes has been extensively studied for both fundamental and technological reasons.¹ For example, investigations of water confinement in the cavities of proteins have provided insight into the molecular functions of proteins.² Alternatively, investigations of the flow of water and solvents through membranes containing nanotubes have suggested that separation is a possibility for use in desalination and water purification.^{3–5} In general, the precise nanoscopic engineering of chemically functionalized and tailored structures of nonpolar

pores is an important aspect in realizing nanofluidic devices. The formation of water clusters in nanoscopic nonpolar pores has been theoretically studied by Vaitheswaran et al.⁶ They examined, for instance, the confinement of water clusters in large pores (0.9–1 nm), and they found that in nonpolar pores the formation of dimers and larger clusters is more favorable than that of dispersed single water molecules. In general, the study of the agglomeration properties of water molecules in

Received: January 22, 2013

Published: June 27, 2013

confined environments is a subject of great interest in the scientific community.^{6–19}

In this study, we investigate the formation of water clusters in the sub-nanometer pores (<0.5 nm) in well-defined and ordered hydrophobic cavities of a fluorinated metal organic framework, FMOF-1. MOFs exhibit high porosity with large surface areas in crystalline and tailorabile structures. MOFs have emerged as attractive materials in many fields, including but not limited to gas separation and storage, catalysis, sensing, optoelectronics, and fuel cells.^{20–35} Methane and hydrogen storage represent active areas of research in MOFs toward clean energy applications.^{36–42} In general, their tailorabile structures provide a platform for polymer chemistry and catalysis, with defined catalytic centers and high catalyst loading with prolonged lifetimes.^{43–46} A major disadvantage of these materials, however, is their low hydrothermal and chemical stability, limiting their use in flue gas separation and gas storage applications.^{47–50} Therefore, efforts are being devoted toward rational synthesis of MOFs with higher thermal and chemical stability.^{51–54}

One such effort is the synthesis and study of fluorinated MOFs (FMOFs) wherein all hydrogen atoms are substituted by fluorine atoms in all the ligands rendering perfluorinated pores.^{55–57} These fluorocoated channels are expected to have high thermal stability and high catalytic activity in addition to enhanced hydrophobicity.^{58,59} Due to their superior hydrophobicity, FMOFs such as FMOF-1 and FMOF-2 have demonstrated high volumetric uptake of liquid hydrocarbon vapors relative to water vapor, suggesting their potential use in oil spill treatment.⁴² The hydrophobic cavities of the FMOFs provide an ideal environment for promoting water cluster formation because of the negligible interaction of water molecules with the pore walls, making it possible to investigate the formation and behavior of water clusters. The formation and thermodynamic stability of large water clusters in the FMOF cavities is also of primary importance for facilitating *in situ* studies of complex phenomena specific to atmospheric photochemistry and ultimately with climate change, as reported in previous studies.^{60,61}

Adsorption isotherms give information about the uptake of adsorbents in materials, particularly those that can be incorporated with high density. However, information about the specific interactions cannot be derived merely by using this method, particularly systems with low-uptake properties such as FMOFs. Indeed, the lowest detectable uptake for standard porous materials such as zeolites or activated carbon measured via adsorption isotherms was ca. 10 kg/m³ at sub-20% RH while the highest reading for FMOF-1 was 0.15 kg/m³ at near 100% RH. Vibrational spectroscopy techniques such as infrared (IR) and Raman spectroscopy have shown remarkable sensitivity toward weak interactions of guest molecules in MOFs, hence providing valuable information about the chemical interactions associated with the adsorption process.^{62–70}

In this work, we investigate the incorporation of highly polar water molecules as well as adsorption of nonpolar methane molecules in a perfluorinated MOF system, FMOF-1 ($\text{Ag}_2[\text{Ag}_4\text{Tz}_6]_n$, where Tz = 3,5-bis(trifluoromethyl)[1,2,4-triazolate]) using surface IR and Raman spectroscopy, adsorption isotherm analysis, and first-principle simulations. The FMOF-1 structure shows extended 3D nanotubular open frameworks consisting of six-connected tetrานuclear $[\text{Ag}_4\text{Tz}_6]$ clusters linked by two three-coordinate Ag(I) centers in each

empirical unit. The framework consists of large semi-rectangular-shaped (~12.2 Å × 7.3 Å) interconnected tubes in the *a* and *b* crystallographic axes with hydrophobic cavities coated with CF₃ groups of the perfluorinated ligands. The walls of each channel of the flexible framework consist of diamond-shaped small cavities or “cages” (~ 6.6 Å × 4.9 Å) that are accessible to dynamic adsorption of small guest molecules such as H₂, O₂, and N₂.^{55–57}

Using a combination of *in situ* IR absorption spectroscopy and first-principles vdW-DF calculations, the formation of water clusters is clearly identified in the cavities of FMOF-1. The results strongly support the agglomeration of isolated water molecules and formation of more stable larger clusters.

2. MATERIALS AND METHODS

2.1. Materials Synthesis. FMOF-1 samples were prepared following previously published methods.^{55–57} Activated FMOF-1 powder crystallinity was confirmed via X-ray diffraction and shown to have the same unit cell parameters as the FMOF-1 single crystals. This result was confirmed by comparing the powder XRD pattern of the activated powder with the simulated powder XRD pattern of the single crystals; TGA and IR analyses were also used to aid the activation protocol (see section 3.1 and the Supporting Information).

2.2. IR and Raman Spectroscopy. IR absorption spectroscopy was performed in transmission mode at room temperature using a liquid N₂ cooled MCT-B detector. A crystalline or microcrystalline sample of approximately 8 mg of FMOF-1 was pressed as a pellet onto a KBr support and mounted into a high temperature, high pressure cell (Specac P/NH 5850c). The pellet samples were heated to 120 °C *in situ* under dynamic vacuum (~20 mTorr), to ensure removal of any physisorbed species or remnant solvent molecules from the synthesis. The similarity of the major vibrational modes of the MOF bands in the IR spectrum of the KBr/MOF pressed pellet to that of neat FMOF-1 described previously^{55,57} suggests preservation of material integrity. Even though this configuration has been used successfully for a large number of systems,^{62–64,71} the KBr pellet environment may not be an ideal environment to study hydrophobic materials such as FMOF-1, due to its propensity to adsorb water. We have ruled out, however, contributions from KBr in the work presented here.

Samples for Raman spectroscopy measurements were used as powder without pressing and activated similar to the IR measurements. Raman measurements were performed using a solid state 532 nm laser as radiation source; FMOF-1 is transparent to this wavelength, so neither resonance Raman nor fluorescence interference is expected. The activated sample was loaded into a Linkam FTIR600 cooling/heating stage. A laser power of 10% (1.23 mWatt) was used to ensure no degradation of the samples by the laser.

2.3. Adsorption Measurements. Two apparatuses were used to carry out the adsorption studies: (a) Micromeritics ASAP 2020 Accelerated Surface Area and Porosimetry Analyzer for surface area and pore size determination through adsorption of N₂ at low pressure (up to 1 bar). This analyzer was used for the powder activation optimization. (b) VTI/TA Gravimetric High Pressure Sorption Analyzer for CH₄ adsorption/desorption measurements up to 55 bar at various temperatures. This VTI/TA system has capabilities for ultrahigh vacuum, low-temperature adsorption studies at cryogenic conditions (*via* a temperature cryostat that provides temperature control ±0.5 °C over the -196 to 300 °C range), high-temperature adsorption studies up to 1000 °C, a flow-dosing manifold for high-pressure studies, and a CI Electronics microbalance with 0.1 μg resolution. The isosteric heat of adsorption of methane into activated FMOF-1 microcrystalline powder was derived through an indirect measurement based on a set of isotherms and the Clausius-Clapeyron equation.⁷²

2.4. Theoretical Methods. Fundamental Modes of FMOF Calculations. To guide the experimental IR spectral assignment of the FMOF-1 fundamental modes, gas-phase frequency calculations were performed within the framework of DFT. In the frequency

calculations, the FMOF-1 system was split into two parts, as illustrated in Figure 9. Both parts 1 and 2 were optimized using the B3LYP^{73–75} hybrid functional in conjunction with an effective core potential ECP-31G(d),^{76–78} with addition of a *d*-polarization functions. Structural optimizations of both parts were performed using Gaussian 09,⁷⁹ and the IR spectrum was plotted using GaussView03.⁸⁰

van der Waals Density Functional Calculations. For the simulation of water adsorption in the cavities of the FMOF-1, we again used DFT calculations, but here utilizing the vdW-DF exchange-correlation functional,^{81–83} as implemented in Quantum ESPRESSO.⁸⁴ This particular exchange-correlation functional is capable of capturing van der Waals interactions, which play an important role in water adsorption in MOFs; it has been applied successfully to many van der Waals-rich systems^{85–91} and, in particular, to the study of physisorption of small molecules in MOF materials.^{71,92–94}

The atomic positions and lattice constants of the FMOF were fixed to the experimental values, where $a = b = 13.43 \text{ \AA}$, $c = 39.17 \text{ \AA}$, and $\alpha = \beta = \gamma = 90^\circ$, and whenever possible we made extensive use of symmetry.⁵⁵ Due to the large size of the unit cell ($\text{Ag}_{24}\text{C}_{96}\text{F}_{114}\text{N}_{72}$), the simulations are computationally demanding. For this reason, we used Γ -point calculations with a plane-wave cutoff of 35 Ry and a density cutoff of 350 Ry. For the description of the core electrons, we employed RRKJ⁹⁵ ultrasoft pseudopotentials. The forces on the atoms in the adsorbed molecules were converged to within $5.0 \times 10^{-5} \text{ Ry/Bohr}$. The infrared frequencies of the water cluster at the Γ -point were calculated using the frozen phonon approach, displacing each atomic position by $\pm 0.01 \text{ \AA}$, from which the dynamical matrix was built and diagonalized. Although the IR frequencies of the water cluster adsorbed in the FMOF are useful in identifying real minima in the complex potential energy surface of the FMOF, these values are in very good agreement with those of isolated water clusters recently calculated by Kolb et al.⁹⁶

Adsorption energies were calculated as follows:

$$\Delta E_{\text{ads}}, \Delta E_{\text{lw}} = E_{\text{FMOF-1+W}} - (E_{\text{FMOF-1}} + E_{\text{W}}) \quad (1)$$

Here, $E_{\text{FMOF-1}}$ and E_{W} are the energy contributions of the isolated FMOF-1 and a single H_2O molecule, while $E_{\text{FMOF-1+W}}$ is the energy of the combined system. When water molecules organize and form clusters, E_{W} in eq 1 becomes the energy of the ($n \text{ H}_2\text{O}$) cluster. It is natural to take as a reference the energy E_{W} of the single water molecule in its gas phase. However, it is also possible to take the water molecule out of a whole water network—ideally resembling a configuration in the liquid phase—and put it into the FMOF-1. The energy of a single water molecule in the liquid state may vary significantly, depending on the configuration chosen, such that large statistical sampling becomes necessary. Since we are only interested in capturing the effects of hydrogen bonding on the water molecule in its first coordination shell before inserting it into the FMOF-1, we compare it with the results of an *ab initio* molecular dynamic (AIMD) simulation at 298 K with 32 water molecules. Practically, we equilibrate 32 water molecules for 3 ps (with a time step of 0.25 fs) at 298 K (experimental conditions) using a Born–Oppenheimer AIMD; this was followed by 30 ps production at 298 K within the canonical ensemble (NVT) using the same time step. Note that the MD simulation was run using *vdW-DF* and the same computational settings as for the calculations of adsorption energies (see section 2.4). With these settings we can describe the first solvation sphere of water (see radial distribution in section S5 of the Supporting Information), in excellent agreement with previous experimental and theoretical investigations.^{57–99} We chose the best representative MD snapshot and carried out a single self-consistent energy calculation, whereas we used the energy of liquid water as reference in the calculation of ΔE_{ads} ; we now use ΔE_{lw} of eq 1 as reference.

The confined environment presented by the FMOF-1 cavities affects the water clusters stability. We can express this in terms of the energy as

$$\Delta E = E_{\text{WCL/FMOF-1}} - E_{\text{WCL/vacuum}} \quad (2)$$

where E_{WCL} is the water cluster energy once in the FMOF-1 cavities ($E_{\text{WCL/FMOF-1}}$) or as isolated entity ($E_{\text{WCL/vacuum}}$). Negative values of ΔE indicate that the water cluster prefers the FMOF-1 cavity.

3. RESULTS

3.1. Sample Activation and Spectroscopic Characterization of H_2O Incorporation. *Sample Activation.* Heating the FMOF-1 sample in vacuum is a necessary measure for the removal of any solvents and adsorbed species, as shown in Figures S1–S3 of the Supporting Information (SI) for the single crystal samples and Figures S4–S6 in section S4 of the SI for the microcrystalline powder sample. A simple IR experiment looking at the changes observed as the sample is heated (at 120 °C) in vacuum overnight confirms the removal of water and solvent peaks (Figure S1). Importantly, the powder sample exhibits the same FMOF-1 structure as previously reported according to XRD data (Figure S6)⁵⁵ while Figures S4–S5 verify that the aforementioned sample pretreatment affords very similar surface area and TGA profile as those attained for single crystals.

The amount of water removed from the sample after heating is estimated from the IR measurements and is found to be equivalent to what is introduced into a fully dehydrated system with 6 Torr of water. The estimation is made by comparing the integrated area of the broad IR band in the region 3000–3600 cm^{-1} after introducing 6 Torr of water into an activated FMOF-1 sample. This indicates that any exposure of the sample to additional water before complete dehydration would not increase the amount of water, because the pores are mostly occupied.

Spectroscopic Characterization of Water Incorporation. The isotherms of water performed at room temperature show no detectable adsorption of water by FMOF-1 as compared to zeolite-5A and BPL carbon.⁵⁷ We have therefore compared the amount of incorporated water in FMOF-1 cavities to a standard nonfluorinated MOF, $\text{Cu}(\text{bdc})(\text{ted})_{0.5}$. The comparison was performed by examining the integrated area of the O–H stretching mode of adsorbed water as compared to that in $\text{Cu}(\text{bdc})(\text{ted})_{0.5}$ ($\text{bdc} = 1,4\text{-benzenedicarboxylate}$ and $\text{ted} = \text{triethylenediamine}$) in the (600–4000 cm^{-1}) region after exposure to 3 Torr of water (16% humidity). Figure 1, therefore, shows the IR absorption spectra of adsorbed water into FMOF-1 (black spectrum) and $\text{Cu}(\text{bdc})(\text{ted})_{0.5}$ (blue spectrum). We find that the FMOF-1 sample exhibits only ~5.6% of the amount of water incorporated into an analogous

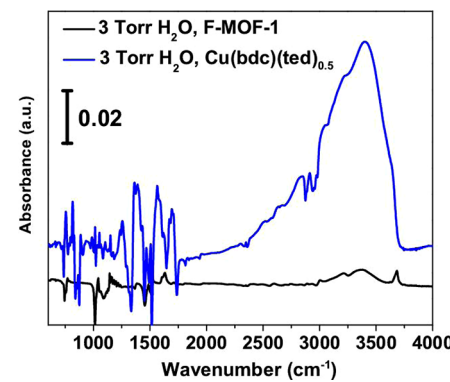


Figure 1. IR absorption spectra of water adsorbed at 3 Torr in blue $\text{Cu}(\text{bdc})(\text{ted})_{0.5}$ and in black FMOF-1.

sample of Cu(bdc)(ted)_{0.5} (Figure 1), which is consistent with the low detection limit of the isotherms (*vide supra*).

To understand the behavior of water cluster formation within the FMOF-1 pores, we performed IR absorption measurements of H₂O vapor in activated FMOF-1 as a function of pressure (800 mTorr to 15 Torr). The bottom part of Figure 2

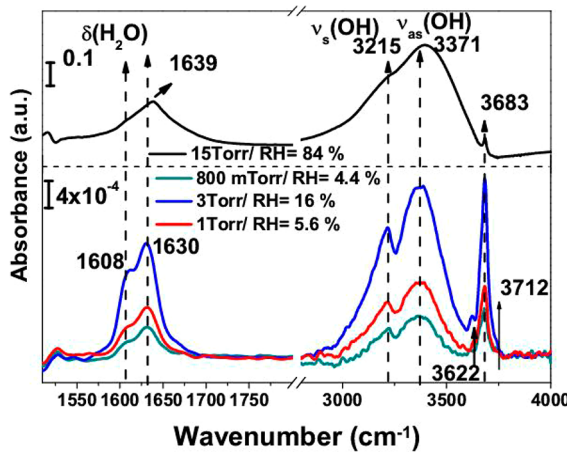


Figure 2. IR absorption spectra of water exposure of FMOF-1 as a function of pressure. Absorption spectra are referenced to dehydrated FMOF-1 in vacuum. Top part shows exposure to 15 Torr; bottom part shows exposure to lower pressures (800 mTorr to 3 Torr).

summarizes the spectra of adsorbed water observed at low water vapor pressures (800 mTorr to 3 Torr), while the top part shows analogous data at a higher pressure (15 Torr). The IR absorption bands in the higher frequency range, centered at 3683, 3622, 3712, 3371, and 3218 cm⁻¹, correspond to the O–H stretching modes of water. The sharp mode centered at 3683 cm⁻¹ can be assigned to a free O–H stretching mode, that is not involved in hydrogen bonding, whereas the two less-intense modes at 3622 and 3712 cm⁻¹ can be assigned to weak hydrogen-bonded water molecules.¹⁰⁰ The modes at 3218 and 3371 cm⁻¹ are assigned to the symmetric and asymmetric stretching modes of strongly hydrogen-bonded water.^{100–102} The IR absorption bands observed in the lower frequency range, at 1630, 1639, and 1606 cm⁻¹, are assigned to the H–O–H scissor modes of H₂O that are both blue- and red-shifted from the unperturbed bending mode of free water at 1621 cm⁻¹.¹⁰³ The width and intensity of the stretching modes of

adsorbed water observed at low water vapor pressures (800 mTorr to 3 Torr)

hydrogen-bonded water molecules are due to H-bonding that leads to an enhancement of the dipole moment of water. In contrast, the scissor mode of water is less affected by hydrogen bonding and, therefore, can be used for quantification of the different water species present.

Examining the pressure dependence of the scissor modes of water as shown in Figure 3 reveals the appearance of two modes at 1606 and 1632 cm⁻¹ observed at lower vapor pressures. As the pressure is increased above ~4 Torr, two new contributions at 1639 and 1676 cm⁻¹ appear.

The right panel of Figure 3 summarizes the integrated area of the scissor modes as a function of pressure, giving the amount present from each contribution. The error bars in integrated areas are found to be $\sim 8 \times 10^{-4}$ cm⁻¹. Fitting the bands as shown in Figure S3 shows that there are many contributions in this range. It can be noted that the largest amount present is due to the bands in the 1630–1640 cm⁻¹ region; the increase after 4 Torr is mainly due to contributions from the 1676 cm⁻¹ attributed to hydrogen-bonded molecules. Changes in the FMOF-1 host vibrational modes are also observed and will be discussed in section 4.2.

vdW-DF Calculations of the FMOF-1/Water Interaction and Cluster Formation. The reactivity of the FMOF-1 toward water was tested using vdW-DF calculations; some water molecules were adsorbed on the exposed principal functionalities of the MOF pores (see Figure 4).

The three main binding groups available in the FMOF-1 nanopores for interaction are as follows: (i) the silver site (Figure 4b), (ii) the fluorine site part of the C–CF₃ groups (Figure 4c), and (iii) hydrogen bridging on the N atoms of the triazole ring (Figure 4c). One water molecule was initially “docked” on each site using the electrostatic complementarity and host–guest principles. After complete coordinate relaxation in each case, summarized in Figure 4a–c, we observed a migration of the water molecules toward the center of the nanopore. Although the adsorption energies are slightly negative with reference to gas-phase water (see ΔE_{ads} , eq 1), they are very small and similar to one another: -23 kJ mol^{-1} for the Ag case (Figure 4b), -24 kJ mol^{-1} for the F site (Figure 4c), and -18 kJ mol^{-1} for the interaction with the triazole ring (Figure 4 d), respectively. Adsorption energies were computed at 0 K and will become weaker as temperature increases; that is, water is more likely to migrate from these sites at higher temperatures, emphasizing the distinct hydrophobicity of this fluorinated MOF.¹⁰⁴ This discussion does not hold when the

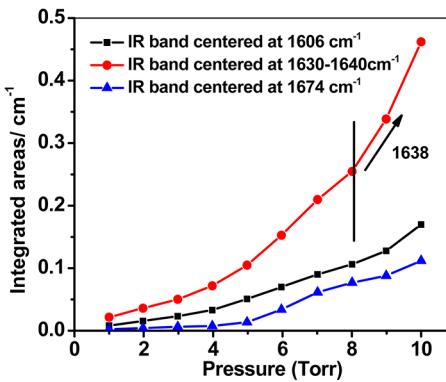
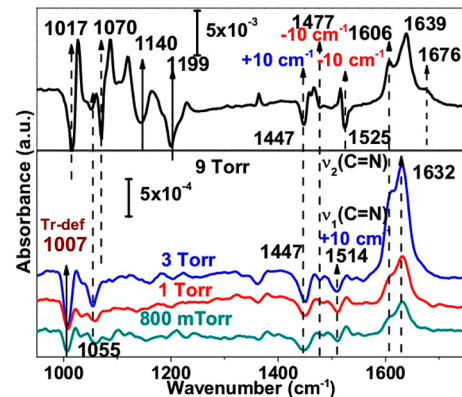


Figure 3. Left: IR absorption spectra of H₂O adsorbed in FMOF-1 showing the bending modes of adsorbed water as a function of pressure. Top part shows IR absorption spectrum at 9 Torr. Right: Integrated area of the bending modes as a function of pressure.

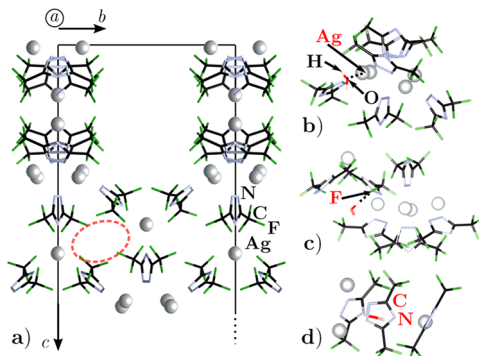


Figure 4. (a) View along the $[0\ 0\ 1]$ plane of FMOF-1. (b–d) show the most relevant adsorption functionalities of FMOF-1, where water molecules were initially adsorbed. The dashed oval in part a) highlights a second, smaller pore of the FMOF-1 structure, here called the “micropore”. (b) Water interacting with silver sites. (c) Water establishing a hydrogen-bond with a fluorine atom. (d) Water docking on top of the triazole ring.

adsorption energy is calculated with water in its change in liquid form as a reference. Water molecules do not favorably “bind” any more, and their ΔE_{lw} values are as follows: +34 kJ mol⁻¹ for the Ag case (Figure 4b), +34 kJ mol⁻¹ for the F site (Figure 4c), and +39 kJ mol⁻¹ for the interaction with the triazole ring (Figure 4d), respectively. Note that the FMOF-1 contains a secondary pore of smaller dimensions, the “micropore” (see Figure 4a). For this case the estimated adsorption energy (ΔE_{ads}) is positive, +2.5 kJ mol⁻¹ (and even more positive for ΔE_{lw}), which would rule out this binding site. However, earlier studies have shown that the FMOF-1 has a flexible structure;⁵⁵ therefore, an induced structural change caused by the presence of water clusters in the large cavity might help the incorporation of a water molecule in the micropore.

Cluster formation in the large pores of the hydrophobic cavities was further studied and compared to their unconstrained form in the gas phase. Their stability was studied as a function of cluster size starting from two water molecules (dimer) up to five (pentamer). Table 1 shows the adsorption

Table 1. Adsorption Energies, Enthalpies, and Free Energies at 298 K (ΔE_{ads} , ΔE_{lw} , ΔH_{ads} , ΔG_{ads}) with Reference to Water in Its Gas-Phase Form and Water Cluster Stability in the FMOF-1 with Respect to Their Gas Phase in kJ mol⁻¹ (ΔE of Eq 2)^a

| | no. H ₂ O | ΔE_{ads} | ΔH_{ads} | ΔG_{ads} | ΔE_{lw} | ΔE |
|----------|----------------------|------------------|------------------|------------------|-----------------|------------|
| dimer | 2 | -30 | -31 | -32 | 17 | -41 |
| trimer | 3 | -34 | -36 | -37 | 12 | -44 |
| tetramer | 4 | -37 | -40 | -42 | 5 | -41 |
| pentamer | 5 | -41 | -46 | -48 | -12 | -62 |

^aNote that ΔE_{lw} was not corrected for thermal effects.

energies ΔE_{ads} and ΔE_{lw} (see eq 1), the enthalpies ΔH_{ads} , and the free energies ΔG_{ads} of H₂O clusters and their relative stabilities, ΔE (see eq 2), in the confined environment shaped by the FMOF-1 nanopores.

Water clusters were designed and reoptimized, with the same level of theory used in section 2.3, starting from previously reported vdW-DF coordinates.⁹⁶ Starting from the optimized gas-phase coordinates, the water clusters were implanted into

the FMOF-1 pore. Figure 5 shows the water clusters considered in our calculations.

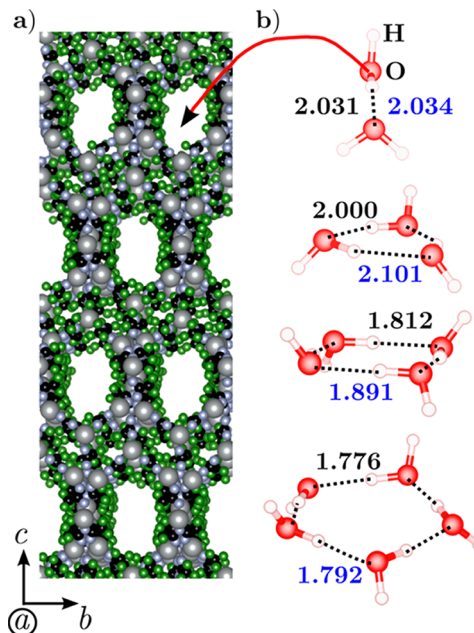


Figure 5. (a) CPK representation of the FMOF-1 where water clusters were introduced and relaxed. (b) Water cluster dimer (top), trimer, tetramer, and pentamer (bottom) with their hydrogen bond distances in the gas phase (black) and inside the FMOF-1 pores (blue). Bond lengths are in Å.

Our initial adsorption calculations indicate that the fluorine atoms are the most reactive sites in the FMOF-1 (see above). We therefore adjusted the hydrogen atoms of the water molecules in contact with fluorine atoms to induce the formation of O–H···F bonds. After complete relaxation of the water cluster coordinates in the rigid FMOF-1 pores, we observed a similar evolution to that of the mono-adsorption case: the water clusters migrate toward the center of the pore. Once again, the water molecules establish a slightly favorable interaction with the FMOF-1 walls (ΔE_{ads} in Table 1) but nonspecific and of a hydrophobic nature. Increasing the cluster size from dimer to pentamer shows a gradual decrease of the adsorption energies originating from a nondirectional dispersive interaction instead of being driven by electrostatic attraction. The effects introduced on the ΔE_{ads} by the zero-point energy, thermal, and entropic contributions (i.e., ΔH_{ads} and ΔG_{ads}) are minimal, not altering the overall picture presented by the ΔE_{ads} of Table 1. In general, when liquid water is used as the reference and ΔE_{lw} calculated (see section 2.3), an opposite trend to that of ΔE_{ads} is observed; that is, small water clusters do not interact favorably with the FMOF-1 walls, while larger water clusters (see e.g. pentamer in Table 1) become more stable, highlighting the contribution of the hydrogen bond to the clusters stability. It is interesting to note that the confinement of the water clusters in the cavities of the FMOF-1 enhances the cluster stability (see ΔE of Table 1). The stability of the cluster increases with cluster size. The internal cluster symmetry is almost completely preserved upon cluster insertion; however, a slight elongation (~1%) of the cluster hydrogen bonds was observed. This effect was found to be more pronounced for larger clusters such as tetramer and pentamer (see Figure 5b).

To identify the size and type of the water clusters present in the FMOF-1 cavities under the conditions of the study, we used the IR frequencies of water scissor (bending) modes derived from ref 81 for clusters of different sizes. This comparison is legitimate for two reasons: (i) the frequency values obtained by Kolb et al.⁹⁶ were calculated with the same level of theory and computational settings used for the result presented in this manuscript; (ii) the symmetry and the geometry of the water cluster, once introduced into the FMOF-1, remain almost unaltered. Figure 6 summarizes the frequency positions of the

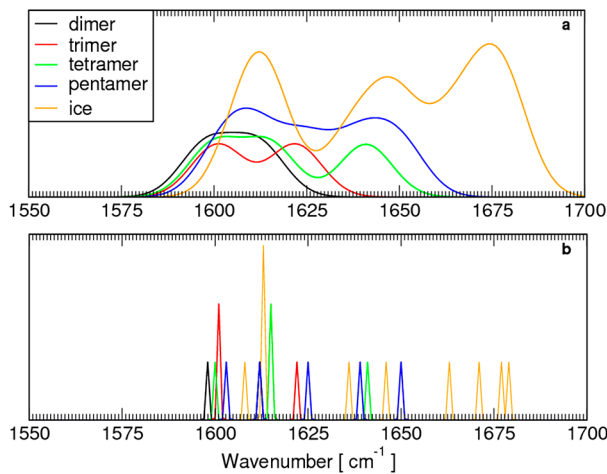


Figure 6. (a) Gaussian convolution (with bandwidth of 20 cm^{-1}) of bending mode frequencies for various cluster sizes. (b) Single frequency values represented by peaks of 1 cm^{-1} width as reported from previous vdW-DF⁹⁶ calculation on gas-phase water clusters.

scissor modes for the different water clusters and ice. The intensities of the peaks were not calculated and set arbitrarily to one (Figure 6a). Panel b of Figure 6 shows the calculated modes convoluted by Gaussian functions of 20 cm^{-1} bandwidth. At first glance, we note that increasing the size of the water clusters increases the number of scissor modes, thereby contributing to the total broadening of the final bands. These frequencies of ice clusters of different sizes (Figure 6a) are then correlated to the observed experimental spectra (Figure 6b) that are clearly structured, in contrast to liquid or adsorbed water. For pressures lower than 3 Torr shown in Figure 3 (bottom panel), we deduce that water clusters contain less than six molecules; that is, clusters with $n > 5$ are not achievable under these conditions. The scissor modes recorded experimentally span the $1600\text{--}1650\text{ cm}^{-1}$ region (Figure 2) that matches the theoretical frequency windows of both the tetramer and pentamer as seen in Figure 6a, b. This finding together with the adsorption energies of Table 1 support the idea that water agglomerates forming relatively small clusters (i.e., much less than the geometrically allowed number). Indeed, within the geometrical volume of the pore, up to 61 molecules could in principle be adsorbed using the stacking (i.e., density) of ice. It appears therefore that the hydrophobicity of the fluorinated walls plays an important role in reducing the size of water clusters.

3.2. Adsorption and Spectroscopic Characterization of Nonpolar CH_4 Interaction in Hydrophobic Cavities. *Adsorption Isotherms of CH_4 .* The methane adsorption isotherms and analysis thereof are shown in Figure 7 for the activated microcrystalline powder of FMOF-1. The lower-

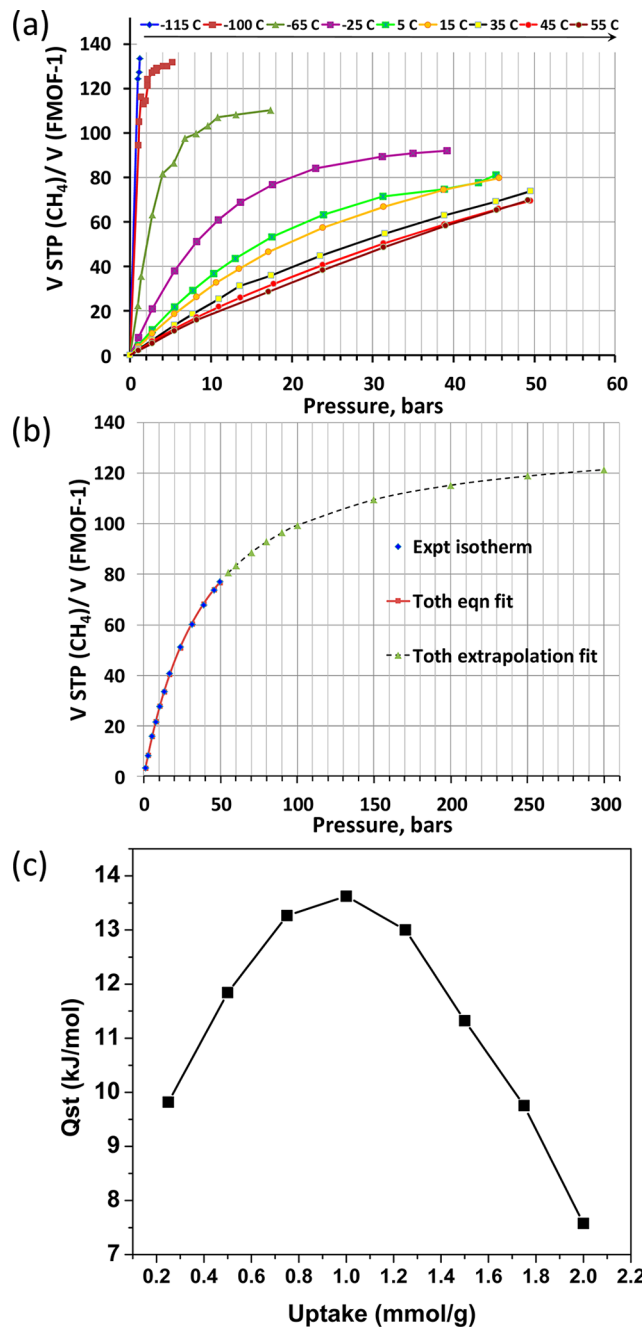


Figure 7. (a) Volumetric uptake of methane adsorption in FMOF-1 as a function of pressure. (b) Toth extrapolation of the room temperature methane isotherm. (c) Isosteric heat of adsorption as a function of methane uptake near ambient temperature (based on isotherm data at 15, 35, and 45 °C).

temperature isotherms show type 1 uptake with a sharp rise that reaches saturation at low pressures whereas the higher-temperature isotherms show an apparently linear behavior without reaching a plateau (Figure 7a). The isotherm at near-ambient temperature (288 K) was fit to the Toth equation,¹⁰⁵ exhibiting excellent agreement with the experimental data and suggesting high compressibility at very high pressures (up to 300 bar) in a manner akin to that exhibited by natural gas cylinders. The projected Toth uptake at 300 bar is approximately two-thirds of the DOE target of 180 V STP/V for methane adsorption, assuming a single-isotherm behavior

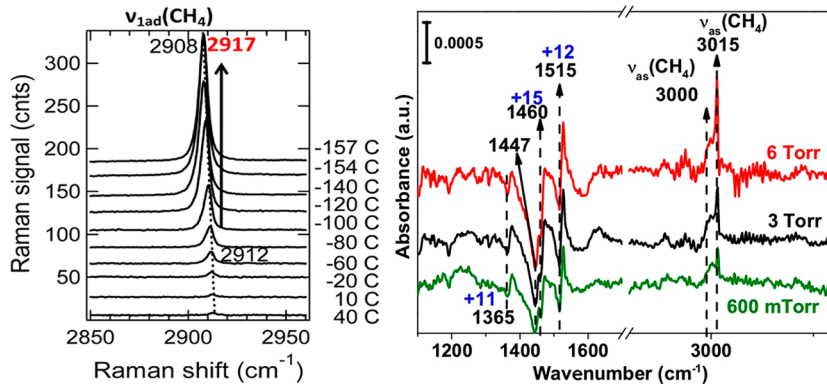


Figure 8. Left: Raman spectra of adsorbed CH₄ as a function of temperature showing the symmetric stretching of CH₄. Right: IR absorption spectra of CH₄ adsorbed into FMOF-1 as a function of pressure.

(Figure 7b). The volumetric adsorption capacities range from 67 V(STP)/V at 288 K and 31 bar to 133 V(STP)/V at 173 K and 5 bar (Figure 7a). These uptakes are significantly lower than analogous values attained by the Zhou group at similar pressures and temperatures for PCN-14, a microporous anthracene-based MOF that exhibits uptakes as high as 230 V STP/V at 290 K and 35 bar with saturation uptake of 434 V STP/V at 125 K.²⁷ Figure 7c shows that an isosteric heat of adsorption of ca. 14 kJ/mol is attained in the higher temperature range near ambient temperature, which is just within the optimum range desired for facile desorption toward vehicular use of compressed fuels.¹⁰⁷

IR and Raman Characterization of CH₄ Adsorption as a Function of Loading. To characterize the interaction of a nonpolar molecule such as CH₄, Raman spectroscopy measurements of CH₄ as a function of temperature were performed. Lowering the temperature represents a way to increase the adsorption in MOFs, as described earlier for N₂ adsorption into FMOF-1 pores.⁵⁶ The sample was loaded at 1 atm and 40 °C and then cooled to -157 °C to increase the uptake, as shown in the left panel of Figure 8. The left panel of Figure 8 summarizes the Raman spectra of FMOF-1 after introducing methane as a function of temperature. As the temperature is lowered to -60 °C, a band at 2912 cm⁻¹ is observed and is attributed to the symmetric stretching of adsorbed CH₄ that is ~-5 cm⁻¹ red-shifted from the unperturbed symmetric stretching of CH₄ at 2917 cm⁻¹. Below -60 °C, this band increases in intensity, an indication that more CH₄ is adsorbed, and the red shift increases to ~-9 cm⁻¹. This suggests that a new IR absorption mode appears and is red-shifted vs the initial absorption band. These modes can be attributed to CH₄ adsorbed into the smaller pores. As the loading is increased (i.e., temperature is lowered), the closer proximity of CH₄ to the framework walls in the "micropores" induces a larger red shift. These results are similar to the behavior of the reported Raman symmetric stretching modes observed for different clathrate cages showing a dependence of the Raman shifts on cage size.¹⁰⁴ IR absorption measurements of methane interaction with FMOF-1 were performed at room temperature as a function of pressure, as summarized in the right panel of Figure 8. The contribution of the methane gas phase was subtracted from the spectra. Two modes, observed at 3015 and 3000 cm⁻¹, are attributed to the asymmetric stretching mode of CH₄. These bands are 2 and 17 cm⁻¹ red-shifted from the unperturbed asymmetric stretching mode of CH₄ at 3017 cm⁻¹. Changes in the FMOF-1 vibration bands in the region (1200–1600 cm⁻¹)

are observed, indicating that there is an interaction with the framework as discussed in section 4.2.

4. DISCUSSION

4.1. Formation of Water Clusters in the FMOF-1 Cavities. The isotherm of water adsorption at room temperature shows negligible adsorption as compared to carbon materials and other zeolites as reported by Yang et al.⁵⁷ Indeed, vdW-DF calculations confirm the weak interaction of the water with the FMOF-1 framework (section 3.1). The detection of molecules using IR spectroscopy is therefore important to explore how water behaves in a confined environment with negligible attractive interactions with the host matrix. The spectroscopy provides details not only on the water interactions with itself and the MOF but also on changes in the MOF bonds themselves, as was reported in earlier work.⁷¹ We focus here on changes obtained for two pressure regimes: lower (800 mTorr to 3 Torr) and higher pressures (~9 Torr).

Interaction at Low Water Vapor Pressure (800 mTorr to 3 Torr). Two scissor modes of adsorbed water are observed at low water vapor pressures, as shown in the bottom part of the left panel of Figure 2. These bands are red- and blue-shifted by ~-15 and ~+18 cm⁻¹ from the unperturbed value of the scissor mode of free water at 1621 cm⁻¹. The 1606 cm⁻¹ IR absorption band is attributed to isolated water molecules, i.e. water molecules not subject to hydrogen bonding, similar to the frequency calculated by Wang et al., for isolated water molecules in carbon nanotubes.¹⁰³ This scissor mode of water is associated with the sharp feature at 3683 cm⁻¹.¹⁰³ This mode can be assigned to an isolated water molecule residing in the *micropore*. Changes in the fundamental IR modes of the FMOF-1 in the large cavity point toward changes that potentially allow access to the micropore, otherwise not possible, as shown by the calculations (section 3.1). Changes in the C–CF₃ stretching mode in the large pores are used below as an indication of water species residing in the vicinity of the fluorine decorated pores.

Both the IR absorption bands at 1606 and 1632 cm⁻¹ are bands shown from the calculation as components of the pentamer water cluster (blue curve Figure 6). The contribution from intramolecular water hydrogen bonding from larger clusters at these pressures is minor, indicated by the smaller intensity of the bending mode of water at 1676 cm⁻¹ at pressures lower than 4 Torr, as shown in the right panel of Figure 3. Information about the effect of incorporation of water clusters in the FMOF-1 cavities can be deduced from the

vibrational modes of the FMOF-1. The vibrational modes of the MOF bands were therefore calculated using DFT, and the results are summarized in Table 2. Examining the behavior of

Table 2. Calculated IR Frequencies of the FMOF-1 Bands for Parts 1 and 2 along with Their Tentative Assignments

| part 1 | freq (cm ⁻¹) | part 2 | freq (cm ⁻¹) |
|---------------------------------------|--------------------------|------------------------------------|--------------------------|
| $\nu(\text{C}-\text{N})$ ring axial-2 | 1516 | $\nu(\text{C}-\text{N})$ of ring | 1477, 1365 |
| $\nu(\text{N}-\text{N})$ vertical | 1074 | triazole ring defo | 1035, 1015 |
| $\nu(\text{C}-\text{N})$ | 1535 | $\nu(\text{N}-\text{N})$ | 1096 |
| vertical | | C-F | 1140 |
| C-F | 1247 | $\text{C}_{\text{tr}}-\text{CF}_3$ | 1447 |

the MOF bands in the bottom part of Figure 3 (left panel) reveals the following changes: (i) $\sim +10 \text{ cm}^{-1}$ blue shift of the band at 1514 cm^{-1} attributed to $\nu(\text{C}-\text{N})$ of the axial triazole ring in part 1 shown in the schematic representation in Figure 9

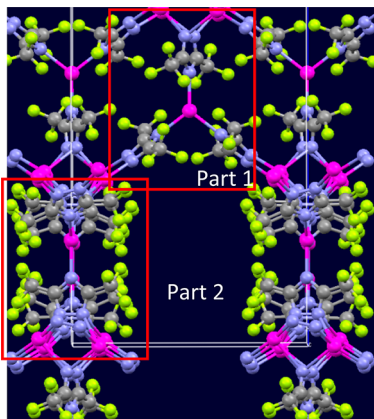


Figure 9. Scheme showing the different parts of the F-MOF-1.

(Table 2), an indication of a perturbation of the C-N of the axial triazole close to site A shown in Figure 10; (ii) a decrease

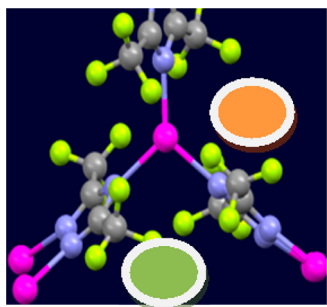


Figure 10. Scheme showing part 1; green oval represents site A and orange oval site B.

in intensity of the mode at 1447 cm^{-1} attributed to the C-CF₃ stretching mode of part 2 shown in Figure 9, along with a decrease in intensity at 1007 cm^{-1} attributed to triazole in part 2 deformation mode indicating the existence of water molecules in the CF₃ vicinity in the large pore (part 2, Figure 9). These observations point to the presence of water molecules in the vicinity of the fluorinated walls and triazole in the *large pore* perturbing the structure at these pressures.

Interaction at High Water Vapor Pressure ($P > 3 \text{ Torr}$). As the pressure is increased, two additional water scissor modes

are observed. These modes are centered at 1639 and 1676 cm^{-1} . The largest blue-shifted scissor mode ($\sim +81 \text{ cm}^{-1}$) is assigned to hydrogen-bonded water molecules (see orange spectrum in Figure 6) or water clusters larger than five water molecules (not calculated here).¹⁰³ Note that a larger number of water scissor modes are observed as the pressure is increased, as shown in Figure S3 in the Supporting Information. The mode observed at $\sim 1639 \text{ cm}^{-1}$ is assigned to the scissor mode of water molecules that are hydrogen bonded (part of water cluster) in the vicinity of the fluorine atoms in the large pores.¹⁰⁶ The slight increase in the integrated area of the mode at 1606 cm^{-1} apparent in the right panel of Figure 3 indicates an increase in the concentration of isolated water molecules in the *micropores*, where the water molecules cannot interact with any other water molecule (mode at 1609 cm^{-1}).

The evolution of the MOF bands is characterized by the following: (i) a $\sim -10 \text{ cm}^{-1}$ red shift in the IR absorption band centered at 1525 cm^{-1} attributed to the $\nu(\text{C}=\text{N})$ stretching mode of the vertical triazole in part 1 shown in Figure 9, part of the *micropores*; (ii) a $\sim -10 \text{ cm}^{-1}$ red shift in the band centered at 1477 cm^{-1} attributed to the $\nu(\text{C}=\text{N})$ of the triazole of part 2, shown in Figure 7; and (iii) a red shift in the IR absorption band at 1140 cm^{-1} attributed to the C-F stretching mode in part 2, only apparent at higher pressures, suggesting the possibility of inducing hydrogen bonding between the water and the fluorine atoms not observed at lower pressures. The experimental observations suggest that, at higher pressures, hydrogen bonding facilitates access to the interior of part 2 close to the triazole ring.

Changes in the MOF vibrational modes at low and higher pressures indicate that the formation of H₂O clusters, most possibly a pentamer cluster under the conditions of the study, starts in the large pores closer to site A in the large cavities. Moreover, they suggest that the framework bonds respond to the presence of water in the cavity, which supports the idea that a slight structural change in the framework would allow water molecules to access the micropores. It is, unfortunately, not possible to obtain detailed unambiguous confirmation from XRD or other measurements to substantiate this conclusion.

4.2. Water Species Stability in the FMOF-1 Pores. The binding strengths of the water clusters in the pores is characterized by examining the desorption rates of the water modes and the behavior of the different water species in the presence of another interacting gas such as methane.

The desorption behavior of each of the water species under reduced pressure (100 mTorr) is summarized in Figure 11. The left panel of Figure 11 shows the integrated area behavior as a function of time upon evacuation to $\sim 100 \text{ mTorr}$, and the right panel shows the normalized integrated areas to the largest value. Comparing the changes in integrated areas of the modes at 1606 and 1641 cm^{-1} at pressure 10 Torr and 100 mtorr (desorption pressure at $t = 0 \text{ min}$) shows that the mode at 1606 cm^{-1} has decreased by 80%, while the mode centered at 1641 cm^{-1} decreased by 58%. This suggests that the 1606 cm^{-1} IR absorption band is associated with the most weakly bound species and is assigned to isolated water molecules or water dimer (black line Figure) in the vicinity of the fluorinated walls. The IR absorption band in the 1630 – 1641 cm^{-1} range arises from contribution of pentamer water clusters formed in the large cavities. vdW-DF calculations (section 3.1) show that the water scissor modes in this range are attributed to water molecules arranged into pentamer water clusters. Therefore, we conclude that the water clusters with larger molecules are more

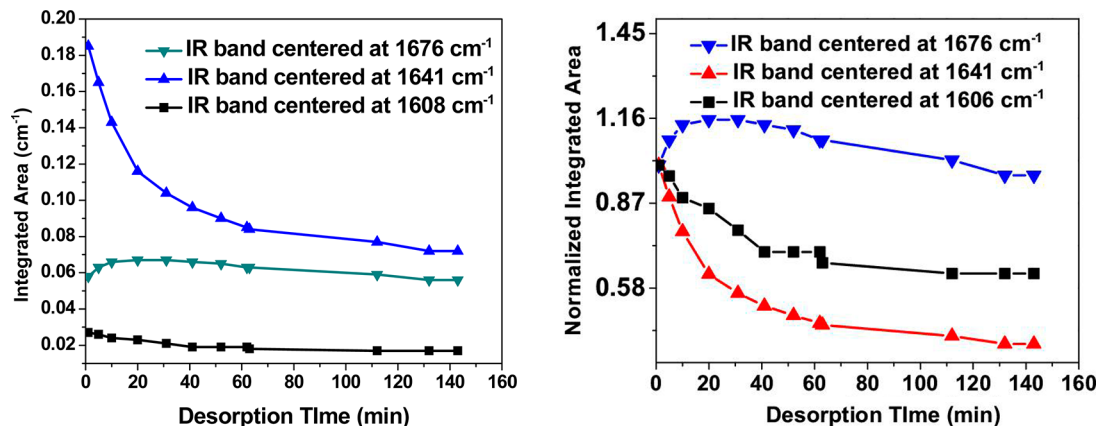


Figure 11. Integrated areas of the bending mode of water in FMOF-1 as a function of desorption time at a pressure below \sim 100 mTorr. The right panel shows the normalized integrated areas to the initial value ($t = 0$ min) of the different bending mode of water as a function desorption time in vacuum ($P = 100$ mTorr).

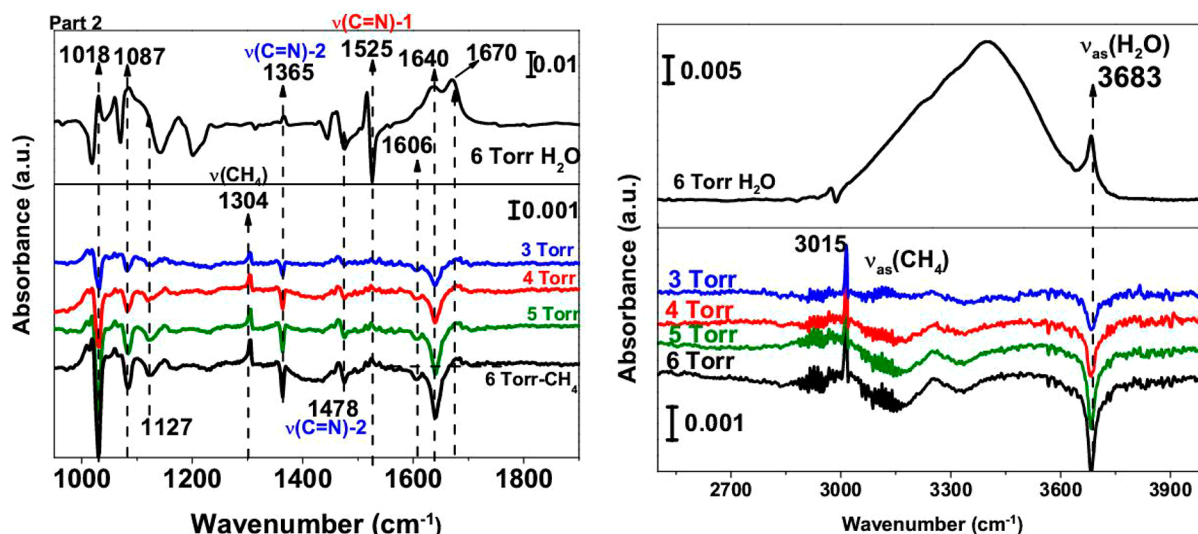


Figure 12. IR absorption spectra of FMOF-1 after exposure to 6 Torr of water referenced to sample in vacuum (top traces) vs corresponding spectra of hydrated FMOF-1 (6 Torr H₂O) after exposure to CH₄ as a function of pressure, referenced to the hydrated FMOF-1 at 6 Torr (bottom traces). The left panel shows the bending modes of adsorbed water, and the right panel shows the stretching mode of adsorbed water.

stable within the pores than isolated or dimerized water molecules. As the desorption time is increased ($t = 140$ min), there is \sim 60% reduction of the integrated area of the mode in the 1630–1641 cm⁻¹ region as counted from the start of the time dependence measurement ($t = 0$ min). An additional \sim 30% reduction in integrated area of the IR absorption band at 1606 cm⁻¹ (from $t = 0$ min) is observed after longer desorption time. This observation supports the interpretation that this band arises from water molecules trapped in the micropores. The intensity of the IR mode at 1676 cm⁻¹, attributed to hydrogen-bonded water molecules (water clusters with more than five molecules), increases as the desorption time is increased. This suggests that the water molecules located close to the fluorinated walls (or in the small pores) are attracted by hydrogen bonding toward the center of the pores and contribute to the mode at 1676 cm⁻¹. In other words, there is a propensity for agglomeration of all remaining water inside the large pores that effectively traps the water molecules, indicating the formation of larger water clusters. Indeed, vdW-DF calculations confirm the higher stability of larger clusters. The formation energies (ΔE in Table 1) also demonstrate a

size-dependence of the cluster—the larger the water cluster, the more likely it is to form—suggesting an agglomeration mechanism within the MOF structure, assuming fast diffusion within the framework. This observation is supported by examining the rate of desorption of the IR absorption OH stretching modes. The modes in the 3000–3500 cm⁻¹ region are removed more slowly than that of the 3683 cm⁻¹ band (see Figure S3 in the Supporting Information).

These results indicate that the hydrogen-bonded water molecules in the large pores are more strongly bound than isolated water species in the vicinity of the fluorine atoms or water interacting with the triazole in the framework, strengthening the suggestion of formation of water clusters in FMOF-1 pores.

In view of the weak interaction between water molecules and the FMOF-1, it is interesting to investigate the effect of other gases on the water clusters present in FMOF-1 pores (e.g., with 6 Torr H₂O). To do so, we first need to examine the interaction of a weakly interacting gas such as methane in the FMOF-1 cavities as discussed below.

Interaction of CH₄ at Low Pressures (600 mTorr to 6 Torr). Figure 7c shows the isosteric heat of methane adsorption onto a FMOF-1 microcrystalline powder sample, indicating the affinity of the FMOF-1 to methane. The information specifics of the interaction can be deduced from IR/Raman spectroscopy. Upon CH₄ loading at room temperature, the main changes in the FMOF-1 IR absorption bands are as follows: (i) ~12 cm⁻¹ blue shift of the band at 1515 cm⁻¹ attributed to $\nu(\text{C}=\text{N})$ of the axial triazole in part 1 shown in Figure 10; (ii) ~15 and ~11 cm⁻¹ blue shifts of the modes centered at 1460 cm⁻¹ and 1365 cm⁻¹, respectively, attributed to the $\nu(\text{C}-\text{N})$ of the triazole of part 2; and (iii) a decrease in intensity of the band at 1447 cm⁻¹ attributed to the C—CF₃ stretching mode of part 2.

These observations reveal that the CH₄ molecules interact mainly with the CF₃ groups in the large pores, possibly due to the large electronegativity of the C—F bonds, with no interaction in the smaller pores at room temperature and low pressures. Raman spectroscopy measurements show that lower temperatures are needed for methane to access the smaller pores (left panel Figure 8). This observation confirms that the interaction of the CH₄ is facilitated through the fluorine decoration at low loading.

Coadsorption. To determine and compare the binding strength of the water species, a controlled amount of methane gas was introduced to a hydrated FMOF-1 (exposed to 6 Torr water) as shown in Figure 12. The top part of Figure 12 (left and right panels) shows the IR absorption spectra of FMOF-1 exposed to 6 Torr of water in the lower frequency (left panel) and in the higher frequency (right panel) ranges. The bottom part in both panels shows the IR absorption spectra of the hydrated FMOF-1 exposed to different pressures of CH₄. The IR spectra are referenced to the hydrated FMOF-1 shown in the top part of Figure 12. The spectra show that, as the hydrated FMOF-1 sample is exposed to methane, some of the water molecules are removed, particularly the modes at 1606, 1641, and 3683 cm⁻¹. An analysis of the dependence of the water modes on methane loading reveals that a slightly larger percentage of the water molecules of the 1606 cm⁻¹ band (~20% at 6 Torr CH₄) is removed as compared to the 1641 cm⁻¹ band (~8% at 6 Torr CH₄). A slight increase in the 1676 cm⁻¹ band, attributed to the hydrogen bonded water molecules in the large pores, is also observed, similar to the phenomenon present during the desorption of water as a function of time. This result serves as additional evidence for the higher stability of the pentamer water clusters that are being formed.

Only the FMOF-1 vibrational modes related to part 2 of the large pore undergo a change. This confirms the assignment of a portion of the 1606 cm⁻¹ IR absorption band to the water in contact with the fluorine decorated walls of the framework; the amount left can be attributed to the water molecules trapped in the small pores, which are not accessible to CH₄ molecules under these conditions.

These observations support the suggestion that the water molecules in the vicinity of the fluorine walls are not as strongly bound to the host and, therefore, allow the penetration of CH₄ between the F-walls and the trapped H-bonded water at the center of the pore. Clearly, hydrogen bonding of water species stabilizes water trapping at the center of the nanopores. The simulations clearly show that the cluster formation is thermodynamically preferred in the hydrophobic walls of the FMOF-1 as compared to the normal gas-phase conditions. The interaction of clusters with the FMOF-1 walls is not driven by the formation of strong hydrogen bonds with the fluorine

atoms available in the FMOF-1 walls; instead, it is dominated by water–water interaction in the pores that are large enough to accommodate clusters, thus helping the preservation of their original shape and symmetry.

Potential Impact for Hydrocarbon Adsorption. The projected Toth uptake at 300 bar is approximately two-thirds of the DOE target of 180 V STP/V for methane adsorption, assuming a single-isotherm behavior (Figure 7b). Multistep isotherms are common in flexible frameworks in general and FMOFs in particular, and that behavior may elevate the experimental uptake to a point at which the DOE limit becomes in sight, but we have not attempted such Toth extrapolations and do not possess the experimental setup to determine methane uptake at the compression pressures needed (300 bar).

As noted above, the volumetric adsorption capacities are significantly lower than analogous values attained by the Zhou group at similar pressures and temperatures for PCN-14, a microporous anthracene-based MOF that exhibits uptakes as high as 230 V STP/V at 290 K and 35 bar with saturation uptake of 434 V STP/V at 125 K.²⁷ Achievement of higher uptake of methane/natural gas-compressed FMOF samples to reach the DOE limit or approach the values attained for PCN-14 may require the design of other FMOF materials with larger pore size than in FMOF-1. (For example, FMOF-2 has approximately double the void size and toluene uptake based on crystallographic values; however, that sample has not yet been activated in a toluene-free form.) Figure 7c shows that an isosteric heat of adsorption of ca. 14 kJ/mol is attained in the higher temperature range near ambient temperature, which is just within the optimum range desired for facile desorption toward vehicular use of compressed fuels.¹⁰⁷

5. CONCLUSIONS

The incorporation of water and formation of water clusters in the hydrophobic cavities of a fluorinated MOF was studied using Raman scattering, IR absorption spectroscopy, and first-principles vdW-DF calculations. Formation of water clusters is deduced by monitoring the frequency shifts of the water molecules and the MOF fundamental vibrational modes.

IR absorption measurements suggest the formation of pentamer water clusters present within the large cavities of the FMOF-1 at low pressures (800 mTorr). Access to the micropores, incorporating an isolated water molecule, is only possible because of the slight modifications of the framework. The interaction with the fluorine-decorated channels is the weakest; instead, hydrogen bonding of the water species dominates, leading to clustering. vdW-DF calculations support the stability of water cluster formation. The hydrophobic environment of the FMOF-1 creates the ideal conditions for the stabilization of these water clusters as compared to the unconstrained case. The delicate balance between nondirectional and nonspecific van der Waals forces and weak hydrogen bonds with the fluorine atoms makes this MOF an interesting platform for studying the formation of water clusters under special conditions. The hydrophobicity of the FMOF-1 and, therefore, the absence of an attractive interaction with water molecules is further confirmed by calculations showing that the absorption energies of single water molecules (or water cluster) on the FMOF walls are much weaker than the intermolecular forces within the clusters stabilized by hydrogen bonds. The possibility of forming and stabilizing various size water clusters in the FMOF-1 cavities opens a path for studying chemical

reactions related to atmospheric aerosols involving reactions of water clusters with sulfuric acid, for example.

Methane adsorption into FMOF-1 is characterized by a volumetric adsorption capacity of 67 V(STP)/V at 288 K and 31 bar with a Toth single-isotherm extrapolation limit projected at \sim 120 V(STP)/V at 300 bar. The experimental (adsorption isotherms and *in situ* vibrational spectroscopy) and computational (molecular and van der Waals density functional simulations) data in this work are consistent with preferential uptake for methane gas relative to water vapor within FMOF-1 pores with ease of desorption and high hydrothermal stability.

■ ASSOCIATED CONTENT

Supporting Information

IR spectra of activation of FMOF-1 in vacuum, integrated areas of the water stretch modes as a function of desorption, fitting of the water modes at 10 Torr, TGA, XRD data, and surface area analysis of FMOF-1. Partial radial distribution of liquid water are also reported. This material is available free of charge via the Internet at <http://pubs.acs.org>.

■ AUTHOR INFORMATION

Corresponding Author

chabal@utdallas.edu; omary@unt.edu

Notes

The authors declare no competing financial interest.

■ ACKNOWLEDGMENTS

The spectroscopic characterization work (performed at UT Dallas in Y.J.C.'s group) and all the theoretical calculations (performed at Wake Forest in T.T.'s group) were fully supported by the Department of Energy, Basic Energy Sciences, Division of Materials Sciences and Engineering (DOE Grant No. DE-FG02-08ER46491). The synthesis and isotherm measurements (performed at UNT in M.A.O.'s group) were supported by the National Science Foundation (CHE-0911690; CMMI-0963509; CHE-0840518) and the Robert A. Welch Foundation (Grant B-1542).

■ REFERENCES

- (1) Rasaiah, J. C.; Garde, S.; Hummer, G. *Annu. Rev. Phys. Chem.* **2008**, *59*, 713.
- (2) Matthews, B. W.; Liu, L. *Protein Sci.* **2009**, *18*, 494.
- (3) Hummer, G.; Rasaiah, J. C.; Noworyta, J. P. *Nature* **2001**, *414*, 188.
- (4) Majumder, M.; Chopra, N.; Andrews, R.; Hinds, B. J. *Nature* **2005**, *438*, 44.
- (5) Srivastava, A.; Srivastava, O. N.; Talapatra, S.; Vajtai, R.; Ajayan, P. M. *Nat. Mater.* **2004**, *3*, 610.
- (6) Vaiteeswaran, S.; Yin, H.; Rasaiah, J. C.; Hummer, G. *Proc. Natl. Acad. Sci. U.S.A.* **2004**, *101*, 17002.
- (7) Brudermann, J.; Lohbrandt, P.; Buck, U.; Buch, V. *Phys. Rev. Lett.* **1998**, *80*, 2821.
- (8) Waal, B. W. v. d. *J. Chem. Phys.* **1987**, *86*, 5660.
- (9) Doye, J. P. K.; Hendy, S. C. *Eur. Phys. J. D* **2003**, *22*, 99.
- (10) Steinbach, C.; Andersson, P.; Kazimirski, J. K.; Buck, U.; Buch, V.; Beu, T. A. *J. Phys. Chem. A* **2004**, *108*, 6165.
- (11) Hirabayashi, S.; Yamada, K. M. T. *J. Mol. Struct.* **2006**, *795*, 78.
- (12) Belau, L.; Wilson, K. R.; Leone, S. R.; Ahmed, M. *J. Phys. Chem. A* **2007**, *111*, 10075.
- (13) Saykally, R. J.; Wales, D. J. *Science* **2012**, *336*, 814.
- (14) Pérez, C.; Muckle, M. T.; Zaleski, D. P.; Seifert, N. A.; Temelso, B.; Shields, G. C.; Kisiel, Z.; Pate, B. H. *Science* **2012**, *336*, 897.

- (15) Waghe, A.; Rasaiah, J. C.; Hummer, G. *J. Chem. Phys.* **2002**, *117*, 10789.
- (16) Devlin, J. P.; Joyce, C.; Buch, V. *J. Phys. Chem. A* **2000**, *104*, 1974.
- (17) Andersson, P.; Steinbach, C.; Buck, U. *Eur. Phys. J. D* **2003**, *24*, 53.
- (18) Abu-samha, M.; Børve, K. J.; Winkler, M.; Harnes, J.; Sætre, L. J.; Lindblad, A.; Bergersen, H.; Öhrwall, G.; Björneholm, O.; Svensson, S. *J. Phys. B: At., Mol. Opt. Phys.* **2009**, *42*, 055201.
- (19) Torchet, G.; Schwartz, P.; Farges, J.; Feraudy, M. F. d.; Raoult, B. *J. Chem. Phys.* **1983**, *79*, 6196.
- (20) Dietzel, P. D. C.; Besikiotis, V.; Blom, R. *J. Mater. Chem.* **2009**, *19*, 7362.
- (21) Demessence, A.; Long, J. R. *Chem.—Eur. J.* **2010**, *16*, 5902.
- (22) Meek, S. T.; Greathouse, J. A.; Allendorf, M. D. *Adv. Mater.* **2011**, *23*, 249.
- (23) Lan, A. J.; Li, K. H.; Wu, H. H.; Kong, L. Z.; Nijem, N.; Olson, D. H.; Emge, T. J.; Chabal, Y. J.; Langreth, D. C.; Hong, M. C.; Li, J. *Inorg. Chem.* **2009**, *48*, 7165.
- (24) Kitagawa, H. *Nat. Chem.* **2009**, *1*, 689.
- (25) Shultz, A. M.; Farha, O. K.; Hupp, J. T.; Nguyen, S. T. *J. Am. Chem. Soc.* **2009**, *131*, 4204.
- (26) Farha, O. K.; Shultz, A. M.; Sarjeant, A. A.; Nguyen, S. T.; Hupp, J. T. *J. Am. Chem. Soc.* **2011**, *133*, 5652.
- (27) Lee, J.; Farha, O. K.; Roberts, J.; Scheidt, K. A.; Nguyen, S. T.; Hupp, J. T. *Chem. Soc. Rev.* **2009**, *38*, 1450.
- (28) Zhou, W. *Chem. Rec.* **2010**, *10*, 200.
- (29) Shekhah, O.; Liu, J.; Fischer, R. A.; Woll, C. *Chem. Soc. Rev.* **2011**, *40*, 1081.
- (30) Kuppler, R. J.; Timmons, D. J.; Fang, Q.-R.; Li, J.-R.; Makal, T. A.; Young, M. D.; Yuan, D.; Zhao, D.; Zhuang, W.; Zhou, H.-C. *Coord. Chem. Rev.* **2009**, *293*, 3042.
- (31) Llabres i Xamena, F. X.; Corma, A.; Garcia, H. *J. Phys. Chem. C* **2006**, *111*, 80.
- (32) Corma, A.; Garcia, H.; Llabres i Xamena, F. X. *Chem. Rev.* **2010**, *110*, 4606.
- (33) Bloch, E. D.; Queen, W. L.; Krishna, R.; Zadrozny, J. M.; Brown, C. M.; Long, J. R. *Science* **2012**, *335*, 1606.
- (34) Lopez, M. G.; Canepa, P.; Thonhauser, T. *J. Chem. Phys.* **2013**, *138*, 154704.
- (35) Canepa, P.; Chabal, Y. J.; Thonhauser, T. *Phys. Rev. B* **2013**, *87*, 094407.
- (36) Eddaoudi, M.; Kim, J.; Rosi, N.; Vodak, D.; Wachter, J.; O'Keeffe, M.; Yaghi, O. M. *Science* **2002**, *295*, 469.
- (37) Wu, H.; Zhou, W.; Yildirim, T. *J. Am. Chem. Soc.* **2009**, *131*, 4995.
- (38) Liu, Y.; Kabbour, H.; Brown, C. M.; Neumann, D. A.; Ahn, C. C. *Langmuir* **2008**, *24*, 4772.
- (39) Senkovska, I.; Kaskel, S. *Microporous Mesoporous Mater.* **2008**, *112*, 108.
- (40) Wu, H.; Zhou, W.; Yildirim, T. *J. Phys. Chem. C* **2009**, *113*, 3029.
- (41) Bao, Z.; Yu, L.; Ren, Q.; Lu, X.; Deng, S. *J. Colloid Interface Sci.* **2011**, *353*, 549.
- (42) Ma, S.; Sun, D.; Simmons, J. M.; Collier, C. D.; Yuan, D.; Zhou, H.-C. *J. Am. Chem. Soc.* **2007**, *130*, 1012.
- (43) Ma, L.; Falkowski, J. M.; Abney, C.; Lin, W. *Nat. Chem.* **2010**, *2*, 838.
- (44) Shultz, A. M.; Sarjeant, A. A.; Farha, O. K.; Hupp, J. T.; Nguyen, S. T. *J. Am. Chem. Soc.* **2011**, *133*, 13252.
- (45) Uemura, T.; Yanai, N.; Kitagawa, S. *Chem. Soc. Rev.* **2009**, *38*, 1228.
- (46) Janssens, N.; Wee, L. H.; Bajpe, S.; Breynaert, E.; Kirschhock, C. E. A.; Martens, J. A. *Chem. Sci.* **2012**, *3*, 1847.
- (47) Kang, I. J.; Khan, N. A.; Haque, E.; Jhung, S. H. *Chem.—Eur. J.* **2011**, *17*, 6437.
- (48) Zhang, L.; Hu, Y. H. *J. Phys. Chem. C* **2010**, *114*, 2566.
- (49) Saha, D.; Deng, S. *J. Phys. Chem. Lett.* **2009**, *1*, 73.
- (50) Cychosz, K. A.; Matzger, A. J. *Langmuir* **2010**, *26*, 17198.

- (51) Ma, S.; Wang, X.-S.; Yuan, D.; Zhou, H.-C. *Angew. Chem., Int. Ed.* **2008**, *47*, 4130.
- (52) Sun, D.; Ma, S.; Ke, Y.; Petersen, T. M.; Zhou, H.-C. *Chem. Commun.* **2005**, 2663.
- (53) Armstrong, G. *Nat. Chem.* **2009**, *1*, 682.
- (54) Low, J. J.; Benin, A. I.; Jakubczak, P.; Abrahamian, J. F.; Faheem, S. A.; Willis, R. R. *J. Am. Chem. Soc.* **2009**, *131*, 15834.
- (55) Yang, C.; Wang, X.; Omary, M. A. *J. Am. Chem. Soc.* **2007**, *129*, 15454.
- (56) Yang, C.; Wang, X.; Omary, M. A. *Angew. Chem., Int. Ed.* **2009**, *48*, 2500.
- (57) Yang, C.; Kaipa, U.; Mather, Q. Z.; Wang, X.; Nesterov, V.; Venero, A. F.; Omary, M. A. *J. Am. Chem. Soc.* **2011**, *133*, 18094.
- (58) Hoang, K. C.; Mecozzi, S. *Langmuir* **2004**, *20*, 7347.
- (59) Furuya, T.; Kamlet, A. S.; Ritter, T. *Nature* **2011**, *473*, 470.
- (60) Pfeilsticker, K.; Lotter, A.; Peters, C.; Basch, H. *Science* **2003**, *300*, 2078.
- (61) Klemperer, W.; Vaida, V. *Proc. Natl. Acad. Sci. U.S.A.* **2006**, *103*, 10584.
- (62) Nijem, N.; Kong, L.; Zhao, Y.; Wu, H.; Li, J.; Langreth, D. C.; Chabal, Y. J. *J. Am. Chem. Soc.* **2011**, *133*, 4782.
- (63) Nijem, N.; Veyan, J.-F.; Kong, L.; Li, K.; Pramanik, S.; Zhao, Y.; Li, J.; Langreth, D.; Chabal, Y. J. *J. Am. Chem. Soc.* **2010**, *132*, 1654.
- (64) Nijem, N.; Veyan, J.-F. o.; Kong, L.; Wu, H.; Zhao, Y.; Li, J.; Langreth, D. C.; Chabal, Y. J. *J. Am. Chem. Soc.* **2010**, *132*, 14834.
- (65) Bordiga, S.; Vitillo, J. G.; Ricchiardi, G.; Regli, L.; Cocina, D.; Zecchina, A.; Arstad, B.; Bjørgen, M.; Hafizovic, J.; Lillerud, K. P. *J. Phys. Chem. B* **2005**, *109*, 18237.
- (66) Hamon, L.; Leclerc, H.; Ghoufi, A.; Oliviero, L.; Travert, A.; Lavallee, J.-C.; Devic, T.; Serre, C.; Ferey, G.; De Weireld, G.; Vimont, A.; Maurin, G. *J. Phys. Chem. C* **2011**, *115*, 2047.
- (67) Canepa, P.; Nijem, N.; Chabal, Y. J.; Thonhauser, T. *Phys. Rev. Lett.* **2013**, *110*, 026102.
- (68) Nijem, N.; Canepa, P.; Kong, L.; Wu, H.; Li, J.; Thonhauser, T.; Chabal, Y. J. *J. Phys.: Condens. Matter* **2012**, *24*, 424203.
- (69) Tan, K.; Nijem, N.; Canepa, P.; Gong, Q.; Li, J.; Thonhauser, T.; Chabal, Y. J. *Chem. Mater.* **2012**, *24*, 3153.
- (70) Nijem, N.; Wu, H.; Canepa, P.; Marti, A.; Balkus, K. J.; Thonhauser, T.; Li, J.; Chabal, Y. J. *J. Am. Chem. Soc.* **2012**, *134*, 15201.
- (71) Nijem, N.; Thissen, P.; Yao, Y.; Longo, R. C.; Roodenko, K.; Wu, H.; Zhao, Y.; Cho, K.; Li, J.; Langreth, D. C.; Chabal, Y. J. *J. Am. Chem. Soc.* **2011**, *133*, 12849.
- (72) Schmitz, B.; Müller, U.; Trukhan, N.; Schubert, M.; Férey, G.; Hirscher, M. *ChemPhysChem* **2008**, *9*, 2181.
- (73) Frisch, M. J.; et al. *Gaussian 03*, Revision C.02; Gaussian, Inc.: Wallingford, CT, 2004.
- (74) Lee, C.; Yang, W.; Parr, R. G. *Phys. Rev. B* **1988**, *37*, 785.
- (75) Becke, A. D. *Phys. Rev. A* **1988**, *38*, 3098.
- (76) Stephens, P. J.; Devlin, F. J.; Chabalowski, C. F.; Frisch, M. J. *J. Phys. Chem.* **1994**, *98*, 11623.
- (77) Stevens, W. J.; Krauss, M.; Basch, H.; Jasien, P. G. *Can. J. Chem.* **1992**, *70*, 612.
- (78) Thomas, R. C.; Walter, J. S. *J. Chem. Phys.* **1993**, *98*, 5555.
- (79) Walter, J. S.; Harold, B.; Morris, K. *J. Chem. Phys.* **1984**, *81*, 6026.
- (80) Dennington, R. II; Keith, T.; Millam, J.; Eppinnett, K.; Hovell, W. L.; Gilliland, R. GaussView; Semichem Inc.: Shawnee Mission, KS, 2003.
- (81) Dion, M.; Rydberg, H.; Schröder, E.; Langreth, D. C.; Lundqvist, B. I. *Phys. Rev. Lett.* **2005**, *95*, 109902.
- (82) Thonhauser, T.; Cooper, V. R.; Li, S.; Puzder, A.; Hyldgaard, P.; Langreth, D. C. *Phys. Rev. B* **2007**, *76*, 125112.
- (83) Langreth, D. C.; Lundqvist, B. I.; Chakarova-Kack, S. D.; Cooper, V. R.; Dion, M.; Hyldgaard, P.; Kelkkanen, A.; Kleis, J.; Kong, L.; Li, S.; Moses, P. G.; Murray, E.; Puzder, A.; Rydberg, H.; Schroder, E.; Thonhauser, T. *J. Phys.: Condens. Matter* **2009**, *21*, 084203.
- (84) Giannozzi, P.; Baroni, S.; Bonini, N.; Calandra, M.; Car, R.; Cavazzoni, C.; Ceresoli, D.; Chiarotti, G. L.; Cococcioni, M.; Dabo, A.; D. C. I.; de Gironcoli, S.; Fabris, S.; Fratesi, G.; Gebauer, R.; Gerstmann, U.; Gougaussis, C.; Kokalj, A.; Lazzeri, M.; Martin-Samos, L.; Marzari, N.; Mauri, F.; Mazzarello, R.; Paolini, S.; Pasquarello, A.; Paulatto, L.; Sbraccia, C.; Scandolo, S.; Sclauzero, G.; Seitsonen, A. P.; Smogunov, A.; Umari, P.; Wentzcovitch, R. M. *J. Phys.: Condens. Matter* **2009**, *21*, 395502.
- (85) Cooper, V. R.; Thonhauser, T.; Puzder, A.; Schröder, E.; Lundqvist, B. I.; Langreth, D. C. *J. Am. Chem. Soc.* **2008**, *130*, 1304.
- (86) Hooper, J.; Cooper, V. R.; Thonhauser, T.; Romero, N. A.; Zerilli, F.; Langreth, D. C. *ChemPhysChem* **2008**, *9*, 891.
- (87) Li, S.; Cooper, V. R.; Thonhauser, T.; Lundqvist, B. I.; Langreth, D. C. *J. Phys. Chem. B* **2009**, *113*, 11166.
- (88) Li, S.; Cooper, V. R.; Thonhauser, T.; Puzder, A.; Langreth, D. C. *J. Phys. Chem. A* **2008**, *112*, 9031.
- (89) Mura, M.; Gulans, A.; Thonhauser, T.; Kantorovich, L. *Phys. Chem. Chem. Phys.* **2010**, *12*, 4759.
- (90) Thonhauser, T.; Puzder, A.; Langreth, D. C. *J. Chem. Phys.* **2006**, *124*, 164106.
- (91) Cooper, V. R.; Thonhauser, T.; Langreth, D. C. *J. Chem. Phys.* **2008**, *128*, 204102.
- (92) Yao, Y.; Nijem, N.; Li, J.; Chabal, Y. J.; Langreth, D. C.; Thonhauser, T. *Phys. Rev. B* **2012**, *85*, 064302.
- (93) Kong, L.; Cooper, V. R.; Nijem, N.; Li, K.; Li, J.; Chabal, Y. J.; Langreth, D. C. *Phys. Rev. B* **2009**, *79*, 081407.
- (94) Kong, L.; Chabal, Y. J.; Langreth, D. C. *Phys. Rev. B* **2011**, *83*, 121402.
- (95) Rappe, A. M.; Rabe, K. M.; Kaxiras, E.; Joannopoulos, J. D. *Phys. Rev. B* **1990**, *41*, 1227.
- (96) Kolb, B.; Thonhauser, T. *Phys. Rev. B* **2011**, *84*, 045116.
- (97) Malcioglu, O. B.; Calzolari, A.; Gebauer, R.; Varsano, D.; Baroni, S. *J. Am. Chem. Soc.* **2011**, *133*, 15425.
- (98) Todorova, T.; Seitsonen, A. P.; Hutter, J.; Kuo, I. F. W.; Mundy, C. *J. Phys. Chem. B* **2005**, *110*, 3685.
- (99) Lin, I. C.; Seitsonen, A. P.; Tavernelli, I.; Rothlisberger, U. *J. Chem. Theory Comput.* **2012**, *8*, 3902.
- (100) Scatena, L. F.; Richmond, G. L. *J. Phys. Chem. B* **2004**, *108*, 12518.
- (101) Richard, T.; Mercury, L.; Poulet, F. o.; d'Hendecourt, L. *J. Colloid Interface Sci.* **2006**, *304*, 125.
- (102) Estrin, D. A.; Paglieri, L.; Corongiu, G.; Clementi, E. *J. Phys. Chem.* **1996**, *100*, 8701.
- (103) Wang, L.; Zhao, J.; Li, F.; Fang, H.; Lu, J. P. *J. Phys. Chem. C* **2009**, *113*, 5368.
- (104) Ohno, H.; Kida, M.; Sakurai, T.; Iizuka, Y.; Hondoh, T.; Narita, H.; Nagao, J. *ChemPhysChem* **2011**, *11*, 3070.
- (105) Toth, J. *Adsorption, Theory, Modeling, and Analysis*; Marcel Dekker: New York, 2002.
- (106) Ostrowska, J.; Narebska, A. *Colloid Polym. Sci.* **1983**, *261*, 93.
- (107) Yuan, S.; White, D.; Mason, A.; Liu, D.-J. *Int. J. Energy Res.* **2013**, *37*, 732.